Journal of Molecular Structure 1224 (2021) 129077

Contents lists available at ScienceDirect

Journal of Molecular Structure

journal homepage: www.elsevier.com/locate/molstr

Thermal, optical, etching, structural studies and theoretical calculations of [1-(2, 5-Dichloro-benzenesulfonyl)-piperidin-4-yl]-(2,4-difluoro-phenyl)-methanone oxime

C.S. Karthik[a,†], Karthik Kumara[b,†], S. Naveen[c,†,*], L. Mallesha[d], P. Mallu[a], M.V. Deepa Urs[e], N.K. Lokanath[b,*]

[a] Department of Chemistry, Sri Jayachamarajendra College of Engineering, JSS Science and Technology University, Mysuru 570 006, India
[b] Department of Studies in Physics, Manasagangotri, University of Mysore, Mysuru 570 006, India
[c] Department of Physics, Faculty of Engineering and Technology, Jain (Deemed-to-be-University), Bangalore 562 112, India
[d] PG Department of Chemistry, JSS College of Arts, Commerce and Science, Ooty Road, Mysuru 570 025, India
[e] Department of Physics, The National Institute of Engineering, Mysuru 570 008, India

ARTICLE INFO

Article history:
Received 9 April 2020
Revised 5 August 2020
Accepted 12 August 2020

Keywords:
Piperidine
Etching
X-ray crystal structure
Distorted tetrahedron
Hirshfeld surface
Density functional theory

ABSTRACT

The title compound [1-(2,5-Dichloro-benzenesulfonyl)-piperidin-4-yl]-(2,4-difluoro-phenyl)-methanone-oxime was synthesized by the substitution reaction of 2,4-difluorophenyl(piperidin-4-yl)methanone oxime with 2,5-Dichloro-benzenesulfonylchloride. The synthesized compounds were characterized by different spectroscopic techniques. The structure of the compound was confirmed by single crystal X-ray diffraction studies, which revealed that the piperidine ring adopts a chair conformation. The geometry around the S atom is distorted tetrahedral. The structure exhibits both inter and intra molecular hydrogen bonds of the type O—H···O and C—H···O. The crystal structure is also stabilized by C—Cl···π and $\pi\cdots\pi$ interactions. Further, the intermolecular interactions are quantified by Hirshfeld surface analysis. The three dimensional energy framework analysis was carried out and the interaction energies between the molecules were computed. The density functional theory calculation was employed to optimize the structural coordinates and the results substantiate the experimental findings. The HOMO-LUMO energy gap and other electronic parameters of the molecule were evaluated. Further, the reactive sites on the molecular surface were identified using molecular electrostatic potential map. Finally, the thermal properties of the crystals were studied using thermogravimetric analysis which revealed that the structure was stable in the temperature range of 20-170°C.

1. Introduction

Piperidine, a biologically active biogenic amine, is a normal constituent in the brain and urine of mammals and humans. It shows potent nicotine like actions on the peripheral and central nervous systems [1]. It is an essential group of the heterocyclic compound in the field of medicinal chemistry due to its diverse biological activities including anticancer [2], antiviral [3], anti-influenza [4], antidepressant [5], cytotoxic [6], antimicrobial [7] and anticonvulsant [8] activities. A picrate salt of 4-[(E)-(2,4-difluorophenyl)(hydroxyimino)methyl]piperidine structure was elucidated using single crystal X-ray diffraction studies [9]. 2,4-Difluorophenyl(piperidin-4-yl)methanone oxime is an intermediate in the preparation of risperidone. Risperidone contains the functional groups of benzisoxazole and piperidine as a part of its molecular structure. It is a typical antipsychotic agent chemically classified as a benzisoxazole derivative with serotonin-5-HT2 and dopamine-D2 antagonist activity [10]. The risperidone has combined serotonin and dopamine receptor and plays a vital role in the treatment of schizophrenia. This may recur even if the patient has switched to a different antipsychotic [11]. One of the most important organic optoelectronic solids in crystal engineering has received tremendous interest in the past several decades [12]. These are made up of organic conjugated molecules and held together by intermolecular interactions such as hydrogen bonds, pi-pi, or

* Corresponding authors.
E-mail addresses: s.naveen@jainuniversity.ac.in (S. Naveen), lokanath@physics.uni-mysore.ac.in (N.K. Lokanath).
† These authors contributed equally

https://doi.org/10.1016/j.molstruc.2020.129077
0022-2860/

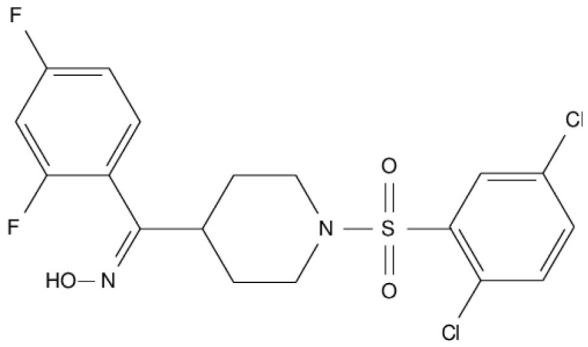

Fig. 1. Schematic diagram of the title compound.

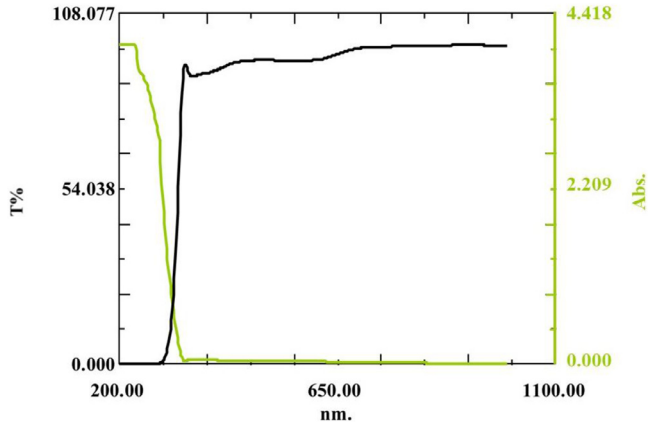

Fig. 3. UV-Vis-NIR spectrum of the title compound (green colour indicates absorption spectra and black colour indicates transmittance spectra).

van der Waals forces. Organic optoelectronic materials are also known as molecular materials exhibiting photonic, electronic, or magnetic properties. A lot of important advancements and achievements have been witnessed on crystal engineering of organic optoelectronic materials [13]. Currently, organic materials receive considerable attention due to their applications in electronic and optoelectronic devices, such as organic thin-film-transistors, light-emitting diodes (OLEDs), organic solar cells, sensors, organic storage, photorefractive devices, and many others [14–17]. In view of their broad spectrum of medicinal and physical properties of the piperidine derivatives, the title compound was synthesized, characterized using different spectroscopic techniques and the molecular structure was confirmed by single crystal X-ray diffraction studies. Further, the Hirshfeld surface analysis and 3D energy frameworks were carried out to understand the molecular interactions and to compute the interaction energies. Furthermore, the density functional theory was employed to understand the electronic and chemical properties of the compound. Finally, the thermogravimetric analysis was carried out to examine the thermal stability of the crystal.

2. Experimental

2.1. Synthesis and crystallization of [1-(2,5-Dichloro-benzenesulfonyl)-piperidin-4-yl]-(2,4-difluoro-phenyl)-methanoneoxime

The title compound was synthesized as per the procedure reported earlier [18]. Single crystals suitable for X-ray diffraction studies were grown from dichloromethane: methanol (3:1) by the slow evaporation of solvent with 73% yield. A schematic diagram of the molecule is shown in Fig. 1. The melting point of the compound is found to be 400-402 K.

To determine the composition and stability of the obtained compound, thermo gravimetric (TG) and differential scanning

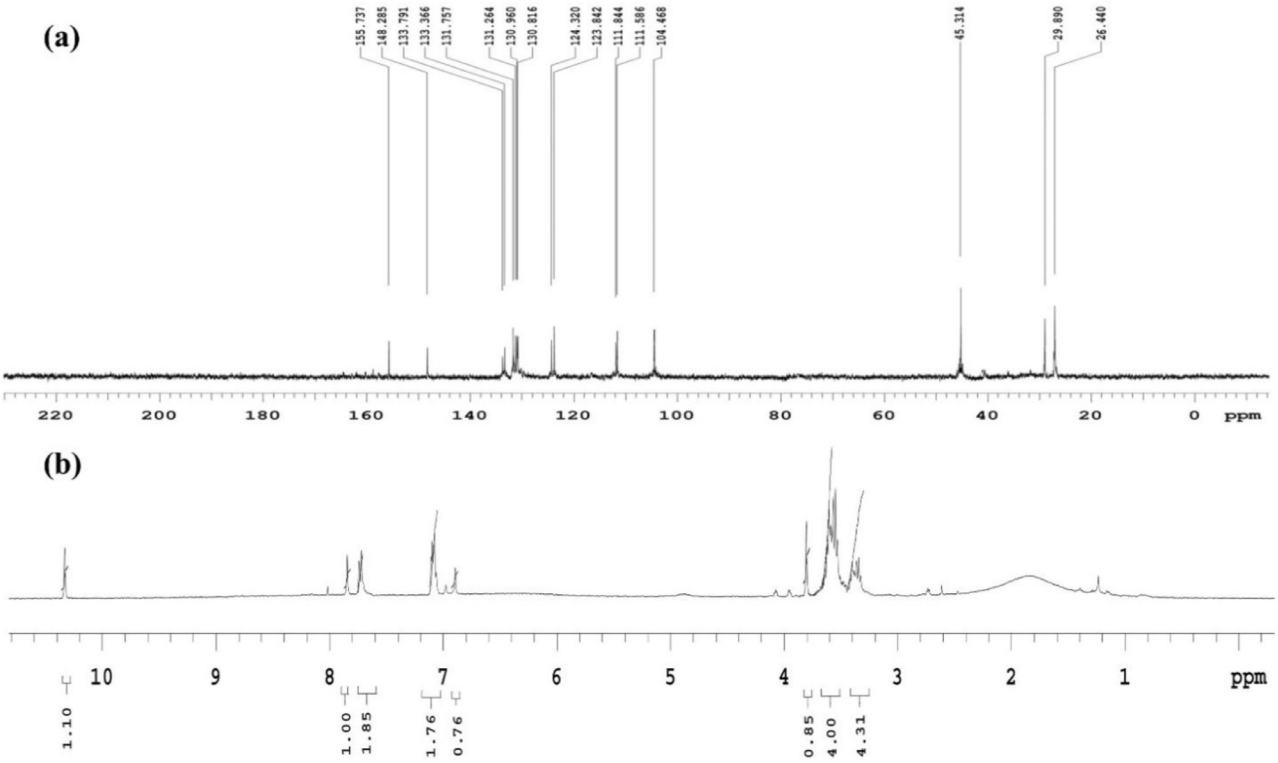

Fig. 2. (a) ^{13}C NMR and (b) ^{1}H NMR spectra of the title compound.

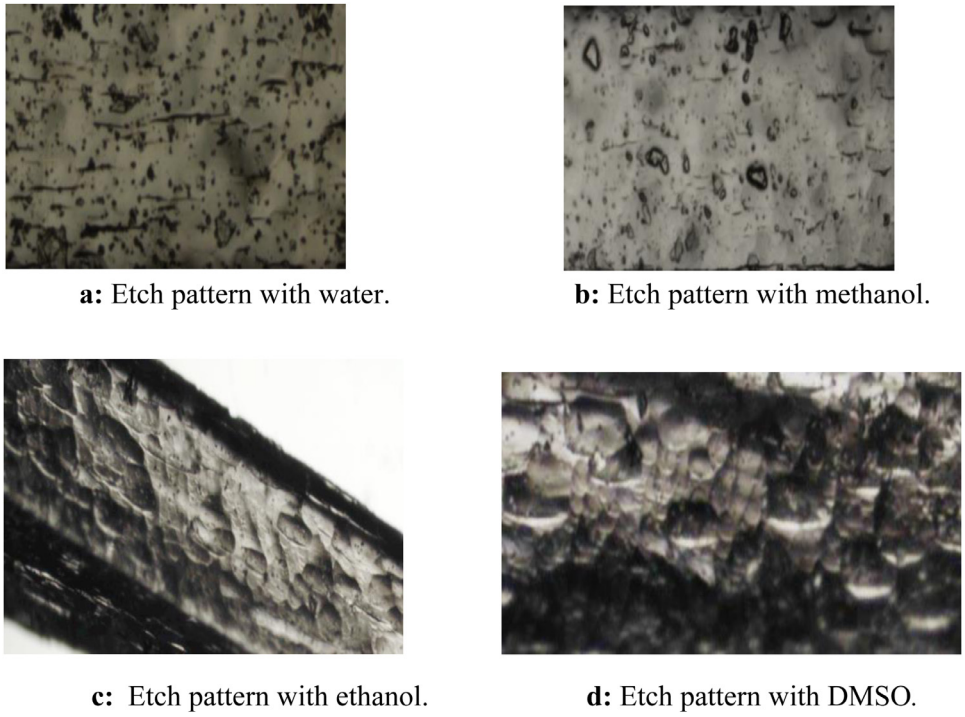

Fig. 4. **a:** Etch pattern with water., **b:** Etch pattern with methanol., **c:** Etch pattern with ethanol., **4d:** Etch pattern with DMSO.

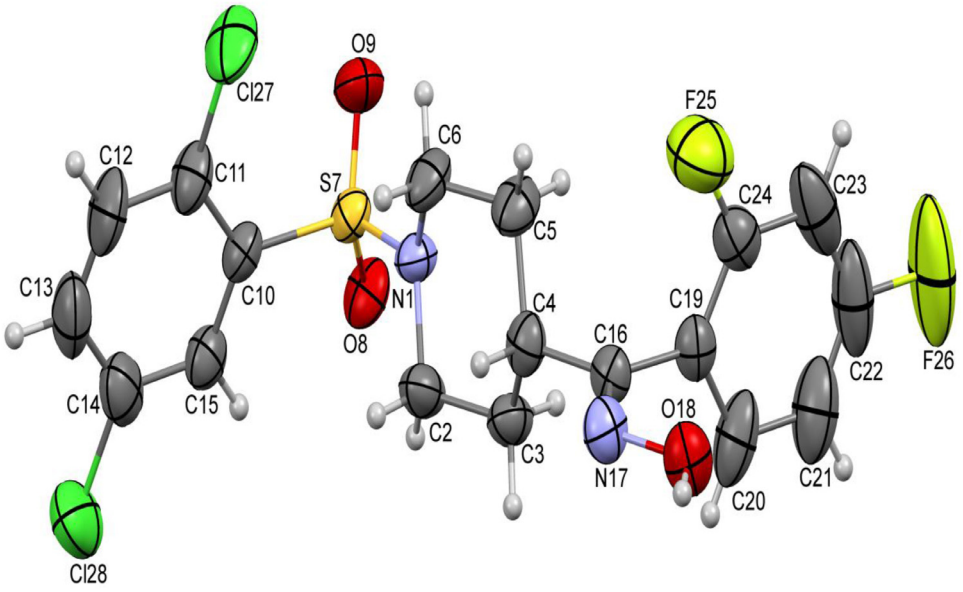

Fig. 5. ORTEP of the molecule with thermal ellipsoids drawn at 50% probability.

calorimetric (DSC) analysis were recorded using a simultaneous TGA Q50 V20.13 and DSC Q200 V.24.11 instruments. Optical absorption and transmission spectrum were recorded in the wavelength range of 200-1100 nm using a UV-Vis-NIR spectrometer. NMR (^{1}H and ^{13}C) spectrum was recorded with an Agilent Instrument operating at 400 MHz with $CDCl_3$ as solvent.

Table 1
Etching behavior of different organic etchants on (3 2 1) surface of grown crystal for 10 seconds.

ETCHANTS	ETCHANT TIME (sec)	CHARACTERISTICS
Water	10	No characteristics pits observed
Methanol	10	Small circular pits observed
Ethanol	10	Dissimilar pits observed
DMSO	10	Deep rectangular pits observed

2.2. Single crystal X-ray diffraction

A colourless block shaped single crystal of dimensions 0.22 × 0.21 × 0.20 mm of the title compound was chosen for an X-ray diffraction study. X-ray intensity data were collected for the title compound at temperature 296 K on a Bruker Proteum2 CCD diffractometer with X-ray generator operating at 45 kV and 10 mA, using CuK_α radiation of wavelength 1.54178 Å. Data were collected

Table 2
Crystal data and structure refinement details.

Parameter	Value
CCDC deposit No.	1025093
Empirical formula	$C_{18}H_{16}Cl_2F_2N_2O_3S$
Formula weight	426.52
Temperature	293(2) K
Wavelength	1.54178 Å
Crystal system, space group	Orthorhombic, $P2_12_12_1$
Unit cell dimensions	a = 8.1657(16) Å, b = 11.3721(18) Å c = 21.314(3) Å
Volume	1979.2(6) Å^3
Z, Calculated density	4, 1.508 Mg/m^3
Absorption coefficient	4.311 mm^{-1}
$F_{(000)}$	920
Crystal size	0.22 × 0.21 × 0.20 mm
Theta range for data collection	4.15° to 64.38°
Limiting indices	-9≤ h ≤ 4, -13≤ k ≤12, -24≤ l ≤24
Reflections collected / unique	8755 / 3167 [R(int) = 0.0459]
Refinement method	Full-matrix least-squares on F^2
Data / restraints / parameters	3167 / 0 / 253
Goodness-of-fit on F^2	1.051
Final R indices [I>2σ(I)]	$R1$ = 0.0524, $wR2$ = 0.1388
R indices (all data)	$R1$ = 0.0568, $wR2$ = 0.1444
Largest diff. peak and hole	0.744 and -0.469 e. Å^{-3}
Flack parameter	0.08(3)

Table 3
Experimental and theoretical comparison of bond lengths (Å).

Bonds	XRD	DFT
N1-C2	1.483(5)	1.4694
N1-C6	1.482(6)	1.4711
N1-S7	1.608(3)	1.6634
C2-C3	1.520(6)	1.5322
C3-C4	1.533(6)	1.5422
C4-C5	1.552(6)	1.5417
C4-C16	1.490(6)	1.5171
C5-C6	1.505(6)	1.5311
S7-O8	1.434(3)	1.4604
S7-O9	1.430(3)	1.4553
S7-C10	1.787(4)	1.8337
C1-C11	1.410(6)	1.4000
C10-C15	1.390(6)	1.3971
C11-C12	1.380(7)	1.3939
C11-Cl27	1.727(5)	1.7498
C12-C13	1.379(9)	1.3897
C13-C14	1.404(8)	1.3904
C14-C15	1.376(6)	1.3886
C14-Cl28	1.730(5)	1.7532
C16-N17	1.293(5)	1.2782
C16-C19	1.496(5)	1.4961
N17-O18	1.410(5)	1.4025
C19-C20	1.416(6)	1.3992
C19-C24	1.367(6)	1.3927
C20-C21	1.385(8)	1.3921
C21-C22	1.37(1)	1.3858
C22-C23	1.37(1)	1.3855
C22-F26	1.367(9)	1.3512
C23-C24	1.365(8)	1.3858
C24-F25	1.311(6)	1.3524
Correlation coefficient (CC)		**0.9903**

Table 4
Experimental and theoretical comparison of bond angles (°).

Angles	XRD	DFT
C2-N1-C6	113.5(3)	115.18
C2-N1-S7	117.3(3)	119.27
C6-N1-S7	120.2(3)	121.86
N1-C2-C3	109.7(3)	109.62
C2-C3-C4	111.4(3)	111.16
C3-C4-C5	108.6(3)	109.72
C3-C4-C16	111.5(3)	112.48
C5-C4-C16	113.9(3)	112.66
C4-C5-C6	111.2(4)	111.06
N1-C6-C5	109.3(4)	109.26
N1-S7-O8	107.1(2)	106.36
N1-S7-O9	108.2(2)	107.45
N1-S7-C10	108.6(2)	108.42
O8-S7-O9	118.5(2)	121.32
O8-S7-C10	104.4(2)	104.13
O9-S7-C10	109.7(2)	108.62
S7-C10-C11	123.7(3)	124.97
S7-C10-C15	116.9(3)	115.6
C11-C10-C15	119.4(4)	119.42
C10-C11-C12	119.8(4)	119.85
C10-C11-Cl27	122.5(3)	123.11
C12-C11-Cl27	117.7(4)	117.04
C12-C13-C14	120.1(5)	119.15
C13-C14-Cl28	120.1(4)	119.69
C15-C14-Cl28	120.2(4)	119.43
C10-C15-C14	120.6(4)	119.98
C4-C16-N17	115.2(3)	115.67
C4-C16-C19	121.9(3)	121.12
N17-C16-C19	122.9(4)	123.21
C16-N17-O18	112.0(3)	112.98
C16-C19-C20	120.1(4)	121.73
C16-C19-C24	121.7(4)	121.19
C20-C19-C24	118.1(4)	117.06
C19-C20-C21	118.1(5)	121.67
C20-C21-C22	120.3(6)	118.3
C21-C22-C23	122.9(7)	122.49
C21-C22-F26	120.7(7)	119.12
C23-C22-F26	116.3(7)	118.39
C22-C23-C24	115.8(7)	117.21
C19-C24-C23	124.7(5)	123.26
C19-C24-F25	118.6(4)	118.93
C23-C24-F25	116.7(5)	117.8
Correlation coefficient (CC)		**0.9733**

for 24 frames per set with different settings of φ (0° and 90°), keeping the scan width of 0.5°, exposure time of 5 s, the sample to detector distance of 45.10 mm and 2θ value at 46.6°. A complete data set was processed using *SAINT PLUS* [19]. The structure was solved by direct methods and refined by full-matrix least squares method on F^2 using *SHELXS* and *SHELXL* programs [20, 21]. All the non-hydrogen atoms were revealed in the first difference Fourier map itself. All hydrogen atoms were positioned geometrically (C–H = 0.93 Å, O–H = 0.82 Å) and refined using a riding model with U_{iso}(H) = 1.2 U_{eq} (C,N) and U_{iso}(H) = 1.5 U_{eq} (O). After several cycles of refinement, the final difference Fourier map showed peaks of no chemical significance and the residual is saturated to 0.0524. The geometrical calculations were carried out using the program *PLATON* [22]. The molecular and packing diagrams were generated using the software *MERCURY* [23].

2.3. Computational studies

The quantum chemical computations were carried out using the density functional theory (DFT) with Gaussian16 software [24] to understand the electronic structure and to explore the possible molecular orbital energies. The structural coordinates were drawn using tools associated with the Gaussian programme, optimized with B3LYP hybrid functional and 6-311G + (d,p) level basis set [25–29] in gas phase. The molecular orbital energies and electronic properties of the compound were computed. The molecular electrostatic potential (MEP) map was plotted to identify the chemical reactive sites on the molecular surface. Further, the molecular orbitals were visualized using Gaussview 6.0.8 [30] without any constraints on the molecular geometry. Furthermore, the different intermolecular interactions involved in the crystal structure were quantified through Hirshfeld surface analysis (HSA) using CrystalExplorer 17.5 [31]. Finally, for the 3D energy framework analysis, the interaction energies between the molecules in the crystalline environment were computed from the monomer wave functions at B3LYP/6–31G(d,p) basis set.

Table 5
Experimental and theoretical comparison of torsion angles (°).

Torsions angles	XRD	DFT
C6-N1-C2-C3	-57.9(4)	-57.75
C2-N1-C6-C5	58.8(4)	58.19
S7-N1-C6-C5	-154.9(3)	-143.65
C2-N1-S7-O9	-175.9(3)	-175.85
C2-N1-S7-O8	-47.1(3)	44.54
C2-N1-S7-C10	65.1(3)	66.93
C6-N1-S7-O9	39.0(4°)	37.85
N1-C2-C3-C4	56.0(4)	54.69
C2-C3-C4-C5	-55.5(4)	-54.77
C2-C3-C4-C16	178.1(3)	178.98
C3-C4-C5-C6	56.6(4)	55.35
C16-C4-C5-C6	-178.5(3)	-178.49
C3-C4-C16-N17	-112.0(4)	-113.89
C3-C4-C16-C19	66.1(5)	65.81
C5-C4-C16-N17	124.6(4)	121.46
C4-C5-C6-N1	-57.5(5)	-55.68
N1-S7-C10-C15	-100.5(3)	-106.86
O8-S7-C10-C11	-163.9(3)	-173.15
O9-S7-C10-C11	-36.0(4)	-42.58
O9-S7-C10-C15	141.4(3)	136.67
S7-C10-C11-C12	178.2(4)	179.39
S7-C10-C11-Cl27	-2.4(6)	-0.38
C15-C10-C11-C12	0.9(7)	0.17
C15-C10-C11-Cl27	-179.7(3)	-179.6
S7-C10-C15-C14	-176.9(4)	-179.71
Cl27-C11-C12-C13	178.3(5)	179.92
C12-C13-C14-Cl28	179.5(5)	-179.85
Cl28-C14-C15-C10	179.1(3)	-179.85
C4-C16-N17-O18	178.4(3)	179.94
C19-C16-N17-O18	0.3(5)	0.26
C4-C16-C19-C20	-93.0(5)	-87.32
C4-C16-C19-C24	88.6(5)	94.13
N17-C16-C19-C20	84.9(5)	92.35
C16-C19-C20-C21	-178.7(5)	-179.23
C16-C19-C24-C23	177.9(5)	179.32
C16-C19-C24-F25	-1.1(6)	-0.66
C20-C19-C24-F25	-179.6(4)	-179.27
C20-C21-C22-C23	0(1)	0.2
C21-C22-C23-C24	-1(1)	-0.13
F26-C22-C23-C24	-179.1(6)	-179.93
C22-C23-C24-F25	-179.9(6)	179.64
Correlation coefficient (CC)		**0.9701**

3. Results and discussion

3.1. NMR analysis

The NMR spectra of the title compound represent the correct number of Carbon and Hydrogen atoms at the appropriate chemical shift values. The NMR (^{13}C and ^{1}H) spectra of the title compound are shown in Fig. 2 (a and b). The strong signals at 148.2 and 133.8 ppm are assigned to the aromatic carbons attached to the fluorine atom. A peak at 133.8 ppm was assigned to the aromatic carbon attached to the sulphur atom (C-S). The aromatic carbon attached to the chlorine atom C-Cl peak was observed in the region 131.8-131.3 ppm. A signal is observed at 45.3 ppm due to carbon atoms in the piperidine (C-N) ring. A strong signal assigned to the carbon atoms in the piperidine ring appears at 29.8 and 26.4 ppm. The peak at 155.7 ppm was assigned to the carbon atom of the oxime. The oxime (-N-OH) proton appears as a singlet peak at 10.312 ppm. The aromatic hydrogens present at carbon atoms C12, C13 in the region 7.72 ppm, C15 in the region 7.85 ppm, C20, C21 in the region 7.08 ppm and C23 in the region 6.84 ppm. The multiplet peaks appeared in the region 3.3 - 3.8 ppm which is assigned to the piperidine protons. The piperidine proton at carbon C4 appears as singlet peak at 3.82 ppm. The triplet peaks appeared in the region 3.52 ppm (C6 and C2 protons) and 3.31 ppm (C5 and C3 protons). The data obtained agree well with the number of carbons, hydrogen's and their chemical shifts with the title compound [32].

3.2. UV-Vis-NIR spectral analysis

The optical absorption and transmission spectra of the solid title compound were recorded by using Agilent Cary 5000 Spectrophotometer shown in Fig. 3. The spectra help to understand the electronic structure and the optical band gap of the crystal. The UV spectra show a wide transparency window, and there is less absorption in the region between 220 and 600 nm, whereas, after 600 to 1100 nm, no absorption was observed. The lower UV cut off wavelength is around 335 nm. The optical band gap energy of the grown crystal was calculated using the formula $E_g = 1240/\lambda$ (nm) in eV, where λ is the lower cut off wavelength (335 nm) [33]. The

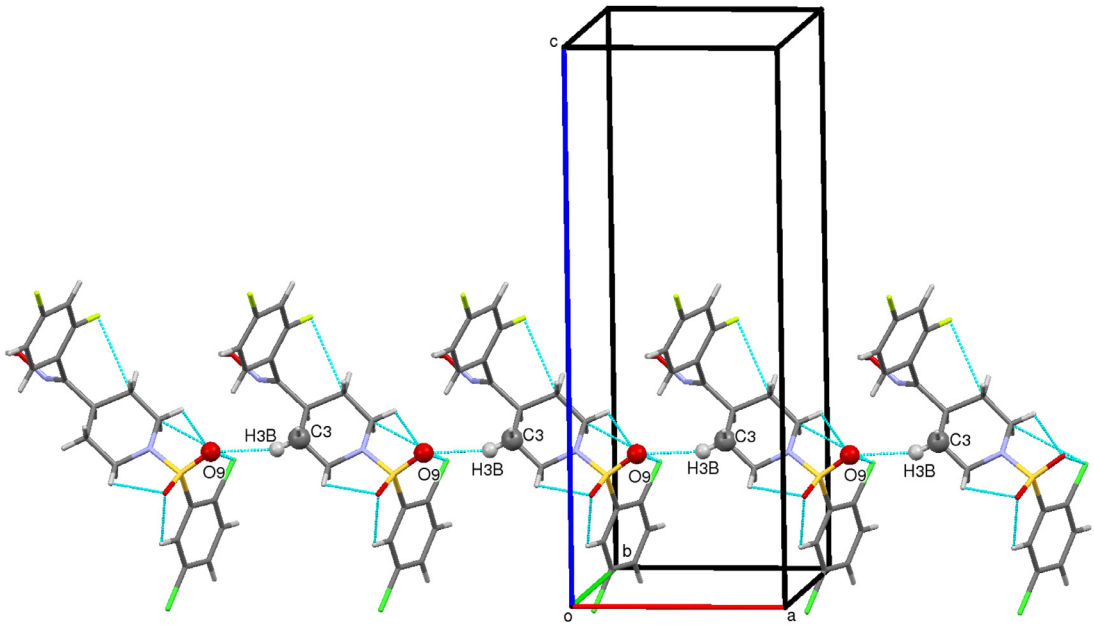

Fig. 6. The packing of the molecules when viewed down the *b*-axis. The dotted lines indicating the C—H···O inter and intramolecular hydrogen bond interactions.

Table 6
The hydrogen bond geometry (Å, °) of the title compound.

D—H···A	D—H	H···A	D···A	D—H···A
O18—H18···O8^{i}	0.82	1.97	2.759 (4)	161
C2—H2A···O8 *	0.97	2.46	2.914 (5)	108
C3—H3B···O9^{ii}	0.97	2.51	3.404 (5)	152
C6—H6B···O9 *	0.97	2.50	2.938 (6)	107
C13—H13···O18^{iii}	0.93	2.57	3.450 (7)	158
C15—H15···O8 *	0.93	2.38	2.793 (5)	106
C23—H23···O18^{iv}	0.93	2.57	3.400 (8)	148

***Intra and Symmetry codes**: (i) -x-1, y+1/2, -z+1/2; (ii) x-1, y, z; (iii) -x-1/2, -y+2, z-1/2; (iv) x+1/2, -y+3/2, -z+1.

band gap of the crystal was found to be 3.70 eV, which is having a wide band gap and high transmittance in the entire visible, near-infrared region, and this property enables the material to hold good for optoelectronic applications [12].

3.3. Surface micromorphology

The etching is an essential characteristic to study the quality of the grown crystals and also it indicates the crystal imperfections and defects [34]. The studies were carried out using water, methanol, ethanol, and DMSO as etchants at room temperature. The good transparent inclusion and cracks free crystal plane (0 0 1) was selected. Fig. 4 (a), (b), (c) and (d) shows the etched patterns of the grown crystal with different time period 10-15s. The crystals were completely immersed in the etchants for 10 s. After dipping for 10-15s, the crystals were cleaned using a tissue paper and the etch patterns were observed using an optical microscope (Motic-02). The etching behaviour of different organic etchants on (3 2 1) surface of the grown crystal is given in Table 1. The etch pit occurred more quickly in the region containing less impurities. The shape of the etch pattern indicates the direction of the dislocation lines [35].

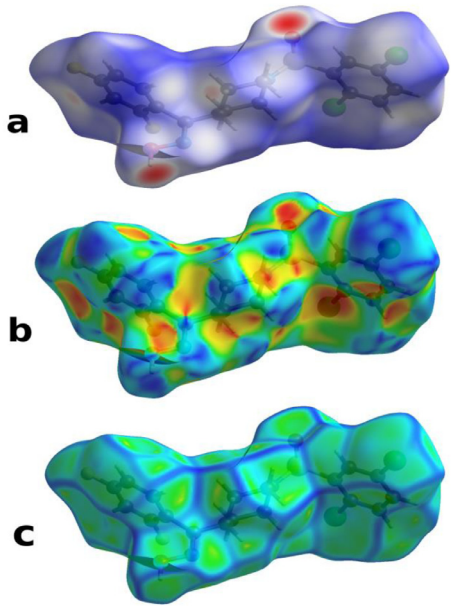

Fig. 8. **(a)** d_{norm}, **(b)** shape index and **(c)** curvedness mapped on Hirshfeld surface of the molecule.

3.4. Crystal structure studies

The crystal structure studies revealed that the title compound crystallized in orthorhombic crystal system with non-centrosymmetric $P2_12_12_1$ space group. The details of the crystal structure and data refinement are given in Table 2. Fig. 5 represents the ORTEP of the molecule with thermal ellipsoids drawn at 50% probability. The list of bond lengths, bond angles and torsion angles of the non-hydrogen atoms are given in Table 3–5 respectively. A study of torsion angles, asymmetric

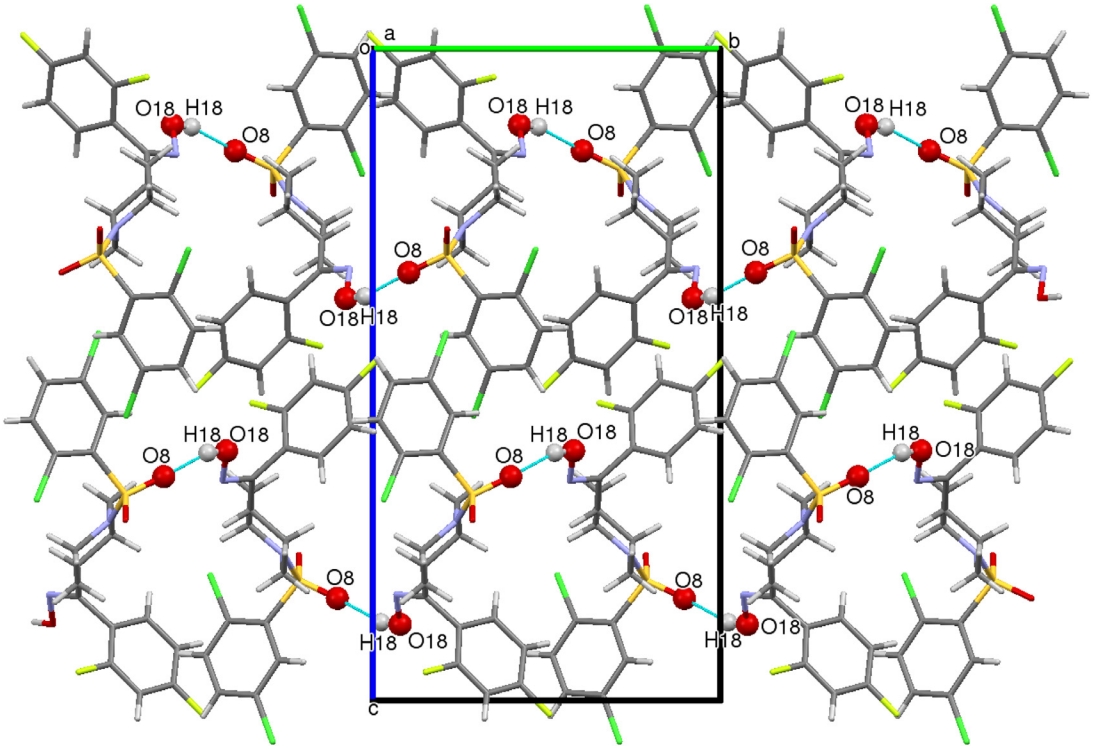

Fig. 7. The packing of the molecules when viewed down the *a*-axis. The dotted lines indicating the O—H···O intermolecular hydrogen bond interactions.

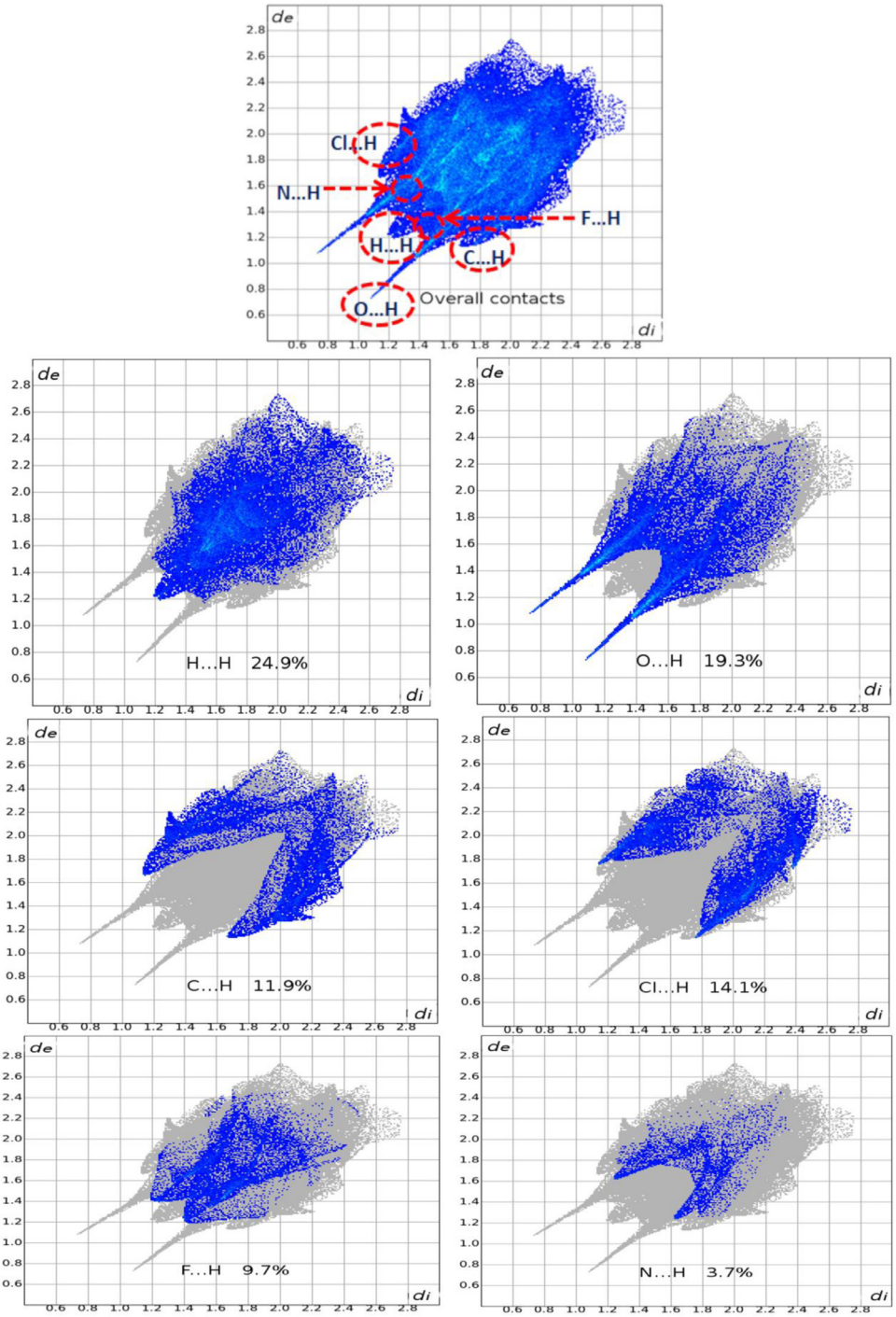

Fig. 9. 2D Fingerprint plots of the title compound showing the individual contribution of each interaction to the total Hirshfeld surface.

parameters and least-square plane calculations reveals that the piperidine ring adopts a chair conformation with the atoms N1 and C4 deviating -0.233(3) Å and 0.242(4) Å respectively from the Cremer and Pople plane [36–37] defined by the atoms C2/C3/C5/C6. This is confirmed by the puckering parameters $Q = 0.581(4)$ Å, $\theta = 1.7(5)^{o}$ and $\varphi = 231(20)^{o}$. The bonds N1-S7 and C4-C17 make an angle 83.58(18)° and 73.8(3)° respectively with the Cremer and Pople plane of the piperidine ring and thus are in the equatorial plane of the piperidine ring. The dihedral angle between the least-squares plane of the piperidine ring and dichlorophenyl ring bridged by the sulfonyl group is 64.7(3)° whereas the piperidine ring makes an angle of 72.8(3)° with the difluorophenyl ring. The dihedral angle between the difluoro and dichlorophenyl rings bridged by the sulfonyl group is 13.2(3)° indicating that they are nearly coplanar. The steric hindrance caused by the bulky sulfonyl group is more than the steric effects caused by the oxime group which are attached on either side of the piperidine ring. This is evident from the bond angle values of 113.5(3)° [DFT:115.18°] and 108.6(3)° [DFT:109.72°] for C6-N1-C2 and C3-C4-C5 respectively. The oxime group bridging the piperidine ring and the diflurophenyl ring is oriented in *+Antiperiplanar* and *+Synperiplanar* conformations as indicated by the torsion angle values of 178.4(3)° [DFT:179.94°] and 0.3(5)° [DFT:0.26°] for C4-C16-N17-O18 and C19-C16-N17-O18 respectively.

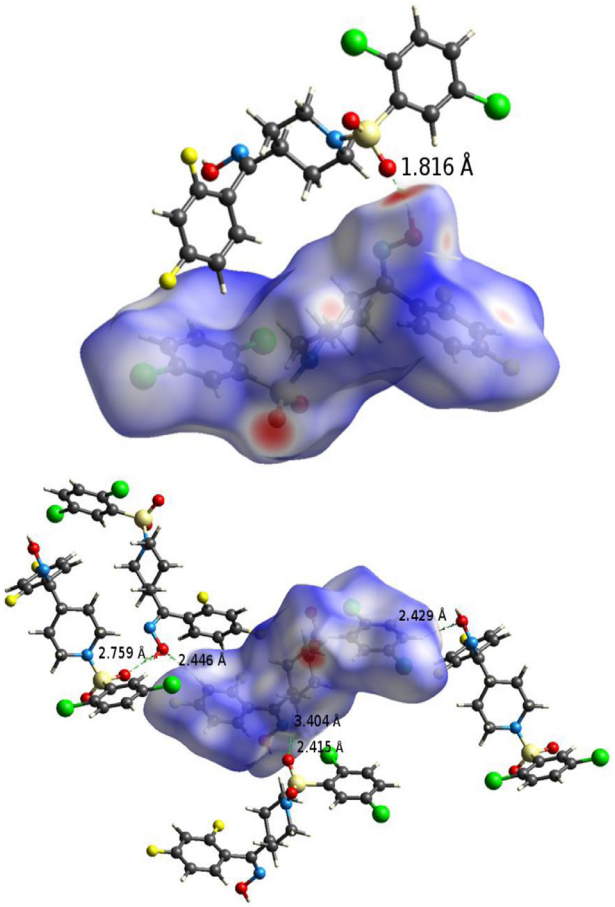

Fig. 10. Visualization of different molecular interactions on Hirshfeld surfaces.

The geometry around the S atom is distorted from regular tetrahedron, with the largest deviation observed for the O-S-O (O9-S7-O8 = 118.5(2)°) [DFT:121.32°] and O-S-N angle [O9-S7-N1 = 108.2(2)°) [DFT:107.45°]. This widening of the angles is due to the repulsive interactions between the S=O bonds and the non-bonded interactions involving the two S-O bonds and the varied steric hindrance of the substituents. The S=O bond distance lies within the expected range of 1.60-1.69 Å. The value of bond angle for N1-S7-C10 is 108.58 (18)° [DFT:108.42°] which is comparable with the ideal tetrahedral value of 109.47° is attributed to the Thorpe-Ingold effect [38]. The sulfonyl O atoms, O8 and O9 adopts *+synclinal* and *-synclinal* conformations as indicated by the torsion angle values of 39.0(4)° [DFT:37.85°] and -47.1(3)° [DFT:-44.54°] for C6-N1-S7-O9 and C2-N1-S7-O8, respectively. The structure exhibits both inter and intramolecular hydrogen bonds of the type O—H···O and C—H···O which play a vital role in stabilizing the crystal structure [39]. The packing of the molecules are shown in Fig. 6 and Fig. 7 indicating layered stacking and are interlinked by the intermolecular (O—H···O and C—H···O) and intramolecular (C—H···O) hydrogen bond interactions to form a polymeric chain like structures. The structure is also stabilized through C—Cl···π and $\pi\cdots\pi$ interactions [40–44]. C(14)—Cl(28) ···Cg(2) interaction with *Cg*(2) is the centroid of the six membered ring (C10/C11/C12/C13/C14/C15) with a C-*Cg* distance of 4.608(6) Å, and C—Cl···Cg angle of 118.76(19)° and the Cl-Cg distance of 3.520(3) Å and a symmetry code of -1/2+*x*, 3/2-*y*, -*z*. The observed hydrogen-bonding geometry of the title compound is listed in Table 6.

3.5. Hirshfeld surface analysis

The Hirshfeld surface analysis (HAS) is an excellent method to understand the intermolecular interactions involved in the crystalline environment. The quantification of the molecular interactions and the visualization of the molecular surface in 2D and 3D plot lead to the clear understanding of the interactions which play an important role in stabilizing the crystal structure. The cif file was used as input and uploaded to CrystalExplorer 17.5 [31] software. The 3D d_{norm} and 2D finger prints on Hirshfeld surfaces (HS) were generated as governed by the Eq. (1), which helps to identify the regions on molecular surface with specific importance. The d_{norm} plots were mapped with colour scale in between −0.615 au (blue) to 1.414 au (red). The d_{norm} on HS with different colour codes indicating the different intermolecular interactions as shown in Fig. 8**.** The coloured regions on the d_{norm} surface represent different intermolecular interactions. Red color with negative d_{norm} indicates the short contacts; white colour with zero d_{norm} indicates the intermolecular distances equal to van der Waals radii, whereas the blue colour with positive d_{norm} indicates the longer contacts [45–46]. The expanded 2D fingerprint plots (FPs) [47–48] for different contacts were displayed in the range of 0.6 - 2.8 Å

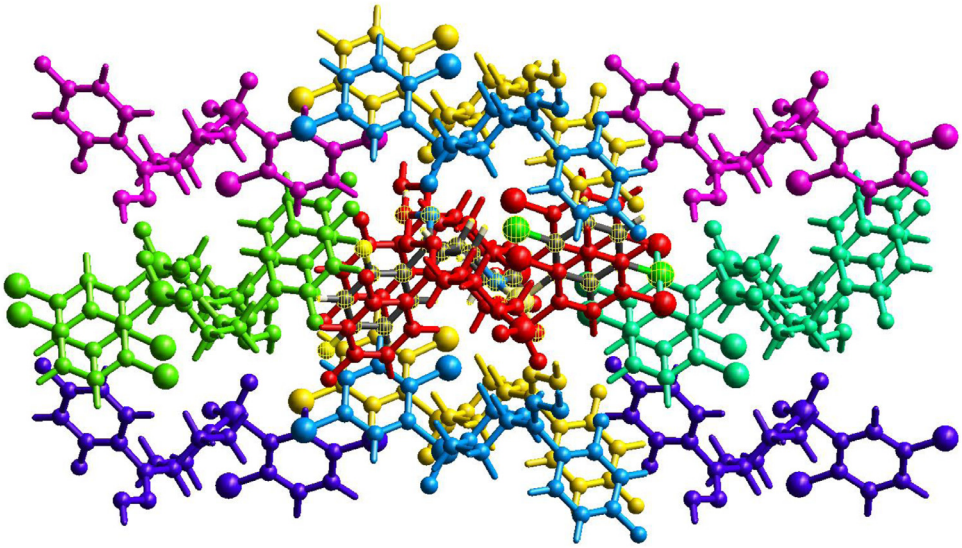

Fig. 11. Molecular cluster of radius 3.8 Å around the selected central molecule.

Table 7
Molecular interaction energies (kJ mol^{-1}) of the cluster of molecules. Each energy should be multiplied by the conversion factors k_{ele} = 1.057, k_{pol} = 0.740, k_{dis} = 0.871, k_{rep} = 0.618 to obtain the total energy (E_{tot}).

Molecule color	*N*	Symop	*R* in Å	E_{ele}	E_{pol}	E_{dis}	E_{rep}	E_{tot}
	2	*x, y, z*	8.17	-14.8	-4.4	-27.2	20.9	-29.7
	2	-*x*, *y*+1/2, -*z*+1/2	7.31	-31	-8.2	-32.6	43.9	-40.1
	2	*x*+1/2, -*y*+1/2, -*z*	11.73	-9.3	-1.1	-20.8	11.1	-21.9
	2	x+1/2, -y+1/2, -z	11.15	-5.9	-0.8	-23	14.2	-18.1
	2	-x, y+1/2, -z+1/2	6.73	-9	-4.4	-35.7	18	-32.7
	2	-x+1/2, -y, z+1/2	12.49	-0.7	-0.5	-9.4	3.4	-7.2
	2	-x+1/2, -y, z+1/2	11.73	-7.3	-1.3	-17.6	12	-16.6

in Fig. 9 with the d_e and d_i distance scales displayed on the graph axes. FPs analysis revealed the contribution of each individual intermolecular contact to the total molecular Hirshfeld surface which can be identified through colour codes ranging from blue through green to red. The red coloured circles on the overall 2D FPs (Fig. 9) represent different intermolecular interactions involved in stabilizing the crystal structure and the corresponding percentage contribution from each interaction. And it is also found that the major contribution is from H···H (24.9%) contact to the total Hirshfeld surface. The inter contacts distance measured with HSA is in good agreement with the experimental value from X-ray structure. Two spikes at d_e and d_i distance in the FPs revealed that the sum of $d_e + d_i$ (1.6+0.7) is 1.816 Å for O···H interactions (Fig. 10). Similarly, other interactions with the corresponding distances are shown in the Fig. 10.

HSA also helps to understand the importance of C–Cl···π and π···π stacking interactions in stabilizing the crystal structure. The shape index (-1.0 au to 1.0 au) and curvedness (-4.0 au to 4.0 au) of the Hirshfeld surface were generated to analyse the π-stacking interactions [49–52] and shown in Fig. 8. The red coloured concave region on the shape index represents the acceptor and the blue region represents the donor atoms. The adjacent red-blue triangles confirmed the presence of the π···π stacking interactions. Similarly, the flat regions on the curvedness (drawn based on the rms value of curvature of the surfaces) indicating the π···π stacking interactions. In sum, the HSA substantiates the presence of interactions observed in X-ray structure.

3.6. 3D energy frameworks and interaction energies

The molecular interaction energies are calculated [29, 53] with the CrystalExplorer software. The molecular cluster (Fig. 11) of radius 3.8 Å around the molecule of interest was generated to calculate the total interaction energy. The energy framework calculations were performed using the symmetry operations to compute the molecular wave functions and to obtain the electron densities of the cluster of molecules present around the selected molecule using the CE-B3LYP/6-31G(d,p) energy model [54] with scale factors to determine E_{tot}: k_{ele} = 1.057, k_{pol} = 0.740, k_{dis} = 0.871, k_{rep} = 0.618. Various intermolecular interaction energies and the total interaction energy between the molecules were also computed with the help of CE-B3LYP/6-31G(d,p) energy model. The total interaction energy is given by

$$E_{tot} = E_{ele} + E_{pol} + E_{dis} + E_{rep} = k_{ele} E'_{ele} + k_{pol} E'_{pol} + k_{dis} E'_{dis} + k_{rep} E'_{rep} \quad (1)$$

Where, E'_{ele} is the classical electrostatic/coulomb energy, E'_{pol} is the polarization energy, E'_{dis} is the dispersion energy and E'_{rep} is the exchange-repulsion energy. And k associated with each energy in the above equation, are the scale factors determined by calibration against quantum mechanical calculation results. Further, obtained interaction energies were used to construct 3D energy frameworks which visualize the packing in the molecular crystal structures [53].

The crystallographic symmetry operations and the corresponding molecular interaction energies (where R is the distance between molecular centroids (mean atomic position) in Å and N is the number of molecules at that distance, energies are in kJ mol^{-1}) are tabulated in Table 7. The dark yellow coloured molecule with symmetry operation (-*x*, *y*+1/2, -*z*+1/2) located at a distance of 7.31 Å from the centroid of the selected molecule has shown the highest total interaction energy of -40.1 kJ mol^{-1}, whereas the dark blue coloured molecule with symmetry operation (-*x*+1/2, -*y*, *z*+1/2) located at a distance of 12.49 Å from the centroid of the selected molecule has shown the lowest total interaction energy (-7.2 kJ mol^{-1}). The total interaction energy (-166.3 kJ mol^{-1}) involving the electrostatic (-82.446 kJ mol^{-1}), polarization (-15.318 kJ mol^{-1}), dispersion (-144.847 kJ mol^{-1}) and repulsion (76.323 kJ mol^{-1}) energy terms were computed using interaction energies between the molecular pairs. The energy frameworks of the compound were generated for electrostatic, dispersion and total energy terms and represented in terms of different coloured cylinders with scale factor (cylinder tube size) 100 and cut off energy -50 kJ/mol. The molecular cluster with red, green and blue coloured cylinders represents the electrostatic energy (E_{elec}), dispersive energy (E_{dis}) and the total interaction energy (E_{tot}) (Fig. 12). The energy framework calculations revealed that the dispersion energy dominates over all other interaction energies in the crystalline environment. The lattice energy of the crystal is found to be -198.5 kJ mol^{-1}.

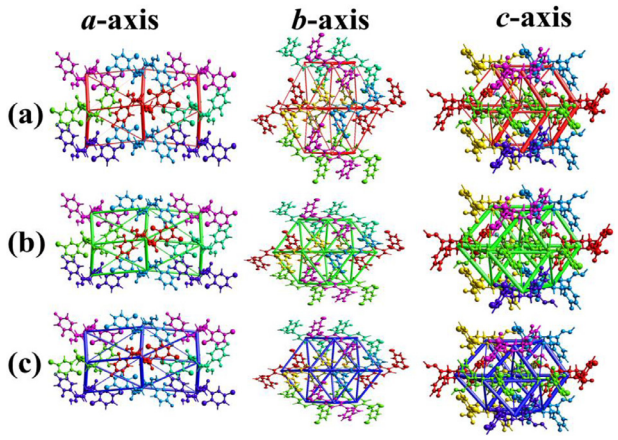

Fig. 12. 3D energy frameworks correspond to **(a)** electrostatic energy, **(b)** dispersion energy and **(c)** total energy of the multicomponent crystals with tube size 100.

Table 8
Calculated frontier molecular orbital energies and electronic properties of the title compound.

Parameters	Value [B3LYP/6-311G(d,p)] (eV)
E_{HOMO}	-7.2279
E_{LUMO}	-1.9092
E_g	5.3187
Ionization potential (I)	7.2279
Electron affinity (A)	1.9092
Electronegativity (χ)	4.5685
Chemical hardness (η)	2.6594
Global softness (σ)	0.3760
Electrophilicity (ω)	3.9241
Chemical potential(μ)	-4.5685
Dipole moment (Debye)	7.0325

where, $\chi = (I+A)/2$, $\eta = (I-A)/2$, $\sigma = 1/\eta$ and $\omega = \mu^2/2\eta$, $E_{g} = E_{LUMO} - E_{HOMO}$.

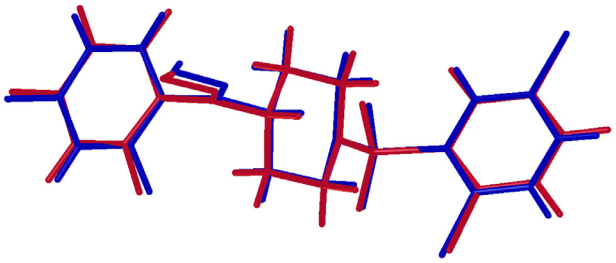

Fig. 14. Structural overlay of the experimental (blue) and DFT (red) structures.

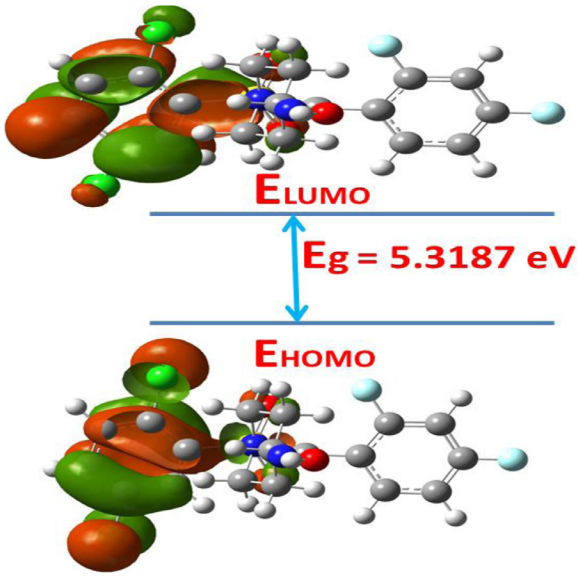

Fig. 15. Frontier molecular orbitals (HOMO-LUMO) with energy gap of the title compound.

3.7. Density functional theory calculations

The electronic properties of the chemical compounds can be understood through the quantum mechanical calculations. The frontier molecular orbital energies and molecular electrostatic potential surface analysis help to identify the chemical active regions. The structural coordinates of the compound are optimized (Fig. 13) in gas phase using DFT method with B3LYP hybrid functional and 6-311+G(d,p) basis set. The optimized structure is compared with the crystal structure and the structural parameters (bond lengths (**CC-0.9903**), bond angles (**CC-0.9733**) and torsion angles (**CC-0.9701**)) of the optimized structures are in good agreement with the experimental findings as confirmed by the correlation coefficient values (Table 3–5). The large variation is observed for the torsion angle values of S7-N1-C6-C5 (-154.9(3)º and -143.65º) and O8-S7-C10-C11 (-163.9(3) º and -173.15º). The structural overlay (Fig. 14) of the two structures obtained from experimental (blue) and DFT (red) was carried out, which results in the

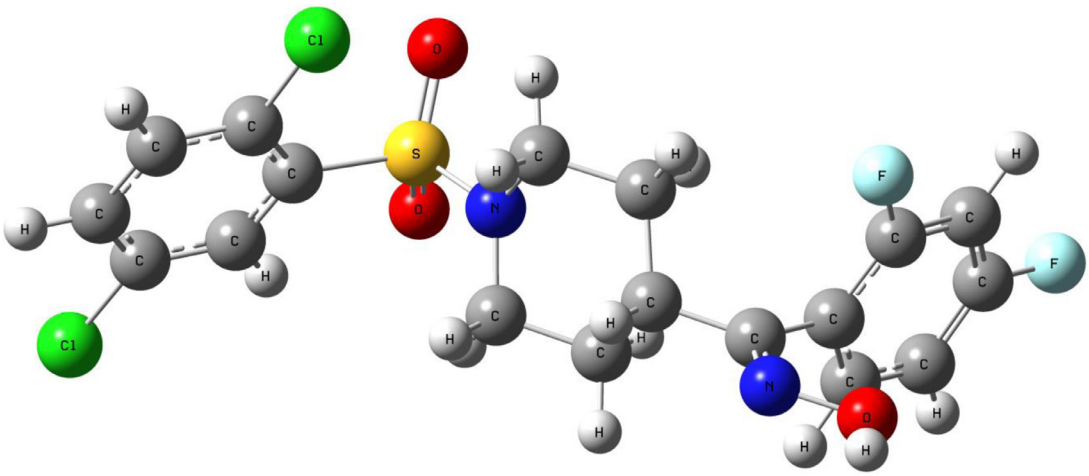

Fig. 13. Optimized structure of the title compound.

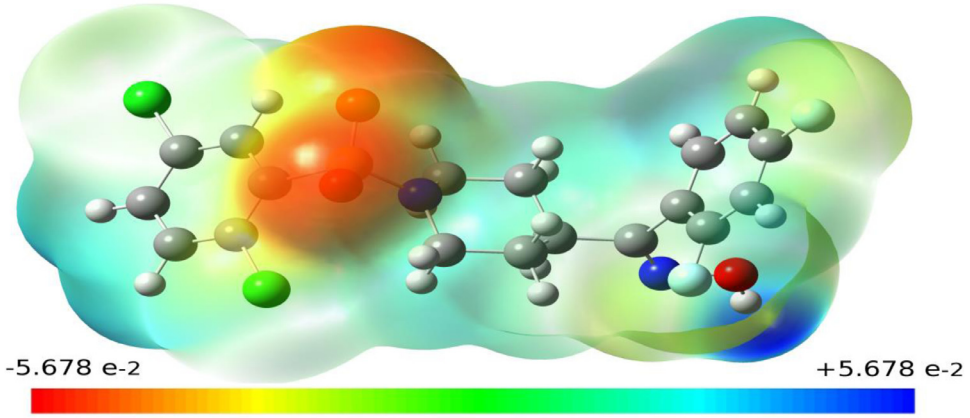

Fig. 16. Molecular electrostatic potential map of the title compound.

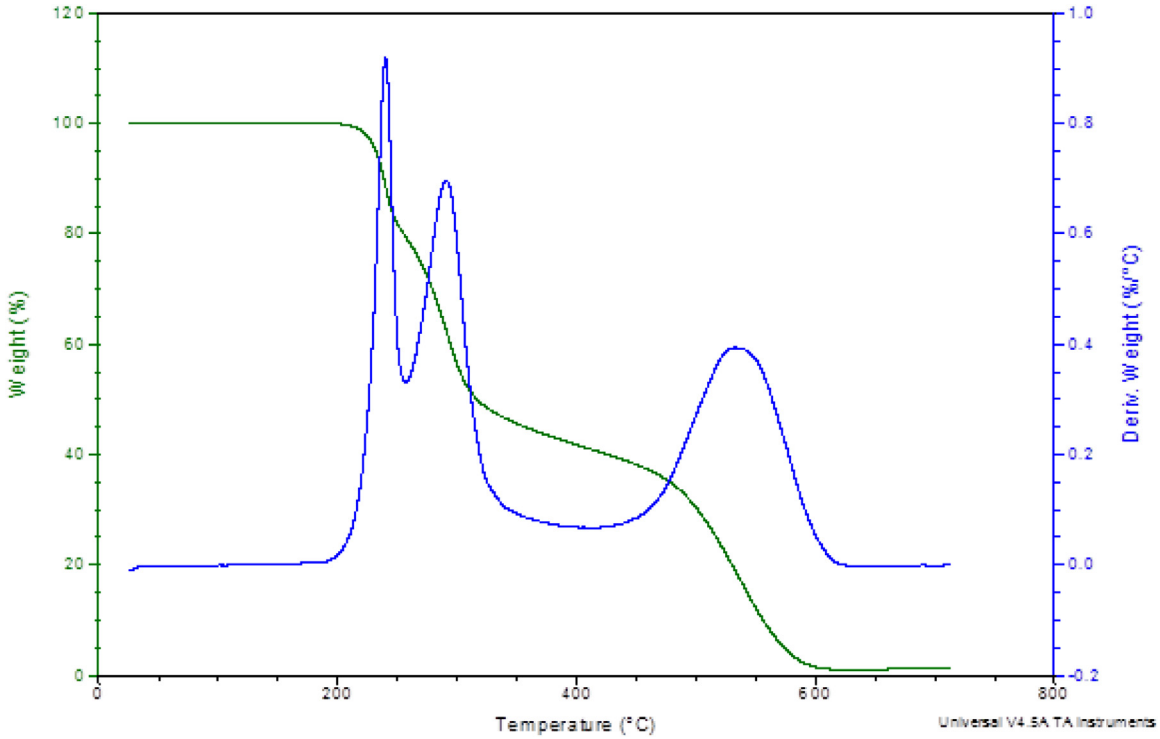

Fig. 17. TGA curve of the title compound.

root mean square deviation value of 0.233 Å, revealed that both the structures are in good agreement except for few values of torsion angles. Further, the energies of the frontier molecular orbitals (E_{HOMO} and E_{LUMO}), energy gap (Eg =5.3187 eV) and associated properties [55–57] such as, ionization energy [$I = E_{HOMO}$], electron affinity [$A = E_{LUMO}$], electronegativity [$\chi = (I + A)/2$], chemical potential [$\mu = (I + A)/2$], global hardness [$\eta = (I - A)/2$], global softness [$s = 1/\eta$] and electrophilicity index [$\omega = \mu^2/2\eta$] are calculated and tabulated in Table 8. The frontier molecular orbitals and HOMO-LUMO energy gap of the compound is shown in Fig. 15. The considerable difference is observed between the calculated energy gap (Eg = 5.3187 eV) using DFT and the experimental energy gap (Eg = 3.70 eV) using UV-visible spectroscopy. The reason for this difference is, the experiment was carried out in the solid phase and the calculation was done in the gas phase. The red and green colours on the molecular surface signify the positive and the negative phases of the wave functions generated. The HOMO LUMO energy gap value of organic molecules plays an important role because they relate to specific movements of electrons. The HOMO behaves as an electron donor and LUMO behaves as an electron acceptor. And also, the polarizability of the molecule is determined based on the energy gap. If the energy gap is smaller, then the compound has more polarizability due to chemical softness. Similarly, the higher energy gap suggests that the compound is less polarizable because of the chemical hardness. The energy gap value of the title compound revealed that the molecule is moderately chemically hard and is less reactive.

The molecular electrostatic potential (MEP) map of the compound is generated in the colour scale range -5.678 e^{-2} au (deepest red) to +5.678 e^{-2} au (deepest blue) and is shown in Fig. 16. The analysis of the MEP map represents charge distribution on the molecular surface. Based on the coloured region on the surface the chemically reactive sites were identified. The positive regions (blue) of MEP represent the electrophilic reactivity, the negative regions (green) related to nucleophilic reactivity of the molecule, and the red regions are related to the electrophilic attack. The MEP

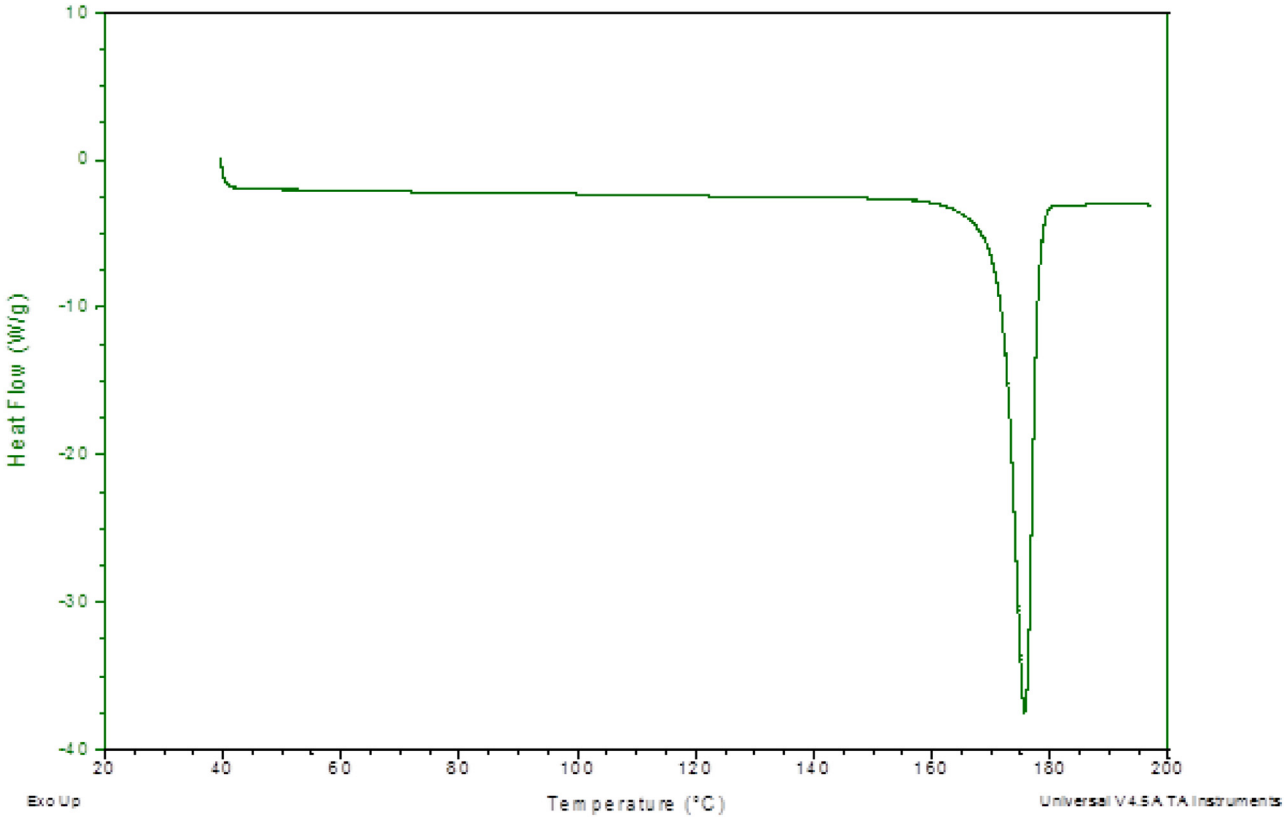

Fig. 18. DSC curve of the title compound.

analysis of the title compound revealed that, the negative regions are concentrated around the oxygen atoms (O8 and O9) of the sulfonyl group with red colour, the light green colour is concentrated over chlorine (Cl27 and Cl28) and fluorine (F25 and F26) atoms, and the blue regions are spread around the hydrogen atoms attached to the carbon atoms and oxygen atom (O18) [55–57].

3.8. Thermal analysis

The sample mass is 10.209 mg for the measurement of TGA over the temperature range of 20 –800°C with a heating rate of 10°C min^{-1} and the sample mass for DSC is 5.8 mg over the temperature range of 20–200°C. The DSC study reveals that no endothermic/exothermic peak is observed below 170°C, suggesting its structure is stable in the temperature range 20 –170°C. The endothermic peak observed in the DSC curve at 176°C represents the melting point of the crystal. From the TG curve, the thermal stability of the sample was studied up to 220 °C, and it shows a loss in weight due to the loosely bound molecules. The TGA curve revealed that the mass loss occurs mainly in five stages. The percentages of mass loss observed in the temperature range 220-254°C, 256-318°C, 318-478°C and 478-612°C are 19.72% (weight loss due to the removal of chlorine and hydroxyl atom), 31.66% (weight loss due to removal of amine and sulfonylbenzene), 30.02% (weight loss due to removal of a fluorine atom and piperidinyl ring), and 17.47%, (weight loss due to removal of phenyl ring) respectively. The remaining mass (1.124%) appears as a residue after 612 °C. The TG and DSC thermograms are shown in Fig. 17 and Fig. 18 respectively.

4. Conclusion

The title compound [1-(2,5-Dichloro-benzenesulfonyl)-piperidin-4-yl]-(2,4-difluoro-phenyl)-methanoneoxime has been synthesized, and confirmed by ^{1}H, and ^{13}C NMR techniques. The single crystal X-ray diffraction studies revealed that the compound is crystallized in orthorhombic crystal system with non-centrosymmetric $P2_12_12_1$ space group. The structure also confirms that the piperidine ring adopts a chair conformation. The geometry around the S atom is distorted tetrahedral. The structure exhibits both inter and intra molecular hydrogen bonds of the type O—H···O and C—H···O which links the molecules to form a three dimensional polymeric chain. The structure is also stabilized through C—Cl···π and π···π interactions. The intermolecular interactions were quantified by Hirshfeld surface analysis, interaction energies between the molecules were computed and the 3D energy frameworks analysis was carried out to understand the molecular interactions. The energy framework analysis revealed that the dispersion energy (-144.847 kJ mol^{-1}) dominate over all other interaction energies. The lattice energy of the crystal is found to be -198.5 kJ mol^{-1}. The density functional theory calculation was employed to optimize the structural coordinates and the results obtained substantiate the experimental findings. The calculated structural parameters are in good agreement with the experimental results as confirmed by the correlation coefficient values of **0.9903, 0.9733 and 0.9701,** and the structural overlay with RMSD value of 0.233 Å. In sum, the results of the crystal structure are substantiated by the results obtained from the Hirshfeld surface analysis and the DFT calculations. The HOMO-LUMO energy gap (5.3187 eV) and other findings of DFT signify the promising electronic properties of the molecule. Further, the reactive sites on the molecular surface were identified using molecular electrostatic potential map. MEP revealed that, the negative regions are concentrated around the oxygen atoms (O8 and O9) and the blue regions are spread around the hydrogen atoms attached to carbon atoms and oxygen atom (O18). Finally, the melting and thermal decomposition temperatures of the crys-

tal were determined using thermogravimetric (TG) and differential scanning calorimetry (DSC) analyses, showed that the structure is stable up to 170°C.

Declaration of Competing Interest

The authors declare that they have no known competing financial interests or personal relationships that could have appeared to influence the work reported in this paper.

CRediT authorship contribution statement

C.S. Karthik: Conceptualization, Data curation, Investigation, Methodology, Writing - original draft, Writing - review & editing. **Karthik Kumara:** Conceptualization, Data curation, Investigation, Methodology, Software, Supervision, Validation, Visualization, Writing - original draft, Writing - review & editing. **S. Naveen:** Conceptualization, Data curation, Project administration, Resources, Writing - original draft, Writing - review & editing. **L. Mallesha:** Formal analysis, Funding acquisition, Investigation, Methodology, Writing - original draft, Writing - review & editing. **P. Mallu:** Formal analysis, Funding acquisition, Project administration, Resources, Writing - original draft, Writing - review & editing. **M.V. Deepa Urs:** Conceptualization, Data curation, Software, Supervision, Validation, Visualization, Writing - original draft, Writing - review & editing. **N.K. Lokanath:** Conceptualization, Data curation, Project administration, Resources, Software, Supervision, Validation, Visualization, Writing - original draft, Writing - review & editing.

Acknowledgments

The authors are grateful to the Institution of Excellence, Vijnana Bhavana and National Single Crystal Diffractometer Facility, Department of Studies in Physics, University of Mysore, Mysuru, India, for providing the X-ray intensity data and computational facilities.

References

[1] M.F. Lockett, Br. J. Pharmacol. Chemother. 4 (1949) 111–119, doi:10.1111/j.1476-5381.1949.tb00523.x.
[2] J.R. Dimmock, M.P. Padmanilayam, R.N. Puthucode, A.J. Nazarali, N.L. Motaganahalli, G.A. Zello, J.W. Quail, E.O. Oloo, H.B. Kraatz, J.S. Prisciak, T. Allen, C.L. Santos, J. Balsarini, E.D. Clercq, E.K. Manavathu, J. Med. Chem. 44 (2001) 586–593, doi:10.1021/jm0002580.
[3] P.E. Finke, B. Oates, S.G. Mills, M. MacCoss, L. Malkowitz, M.S. Springer, S.L. Gould, J.A. Demartino, A. Carella, G. Carver, K. Holmes, R. Danzeisen, D. Hazuda, J. Kessler, J. Lineberger, M. Miller, W.A. Schleif, E.A. Emini, Bioorg. Med. Chem. Lett. 11 (2001) 2475–2479, doi:10.1016/S0960-894X(01)00492-9.
[4] O.I. Yarovaya, A.S. Sokolova, I.Y. Mainagashev, A.S. Volobueva, K. Lantseva, S.S. Borisevich, A.A. Shtro, V.V. Zarubaev, N.F. Salakhutdinov, Synthesis and structure-activity relationships of novel camphecene analogues as anti-influenza agents, Bioorg. Med. Chem. Lett. 29 (23) (2019) 126745.
[5] A.A. Trabaco, N. Aerts, R.M. Alvarez, J.I. Andres, I. Boeckx, J. Fernandez, A. Gomez, F.E. Janssens, J.E. Leenaerts, A.I.D. Lucas, E. Matesanz, T. Steckler, S. Pullan, Bioorg. Med. Chem. Lett. 17 (2007) 3860–3863, doi:10.1016/j.bmcl.2007.05.012.
[6] I. Ninomiya, T. Kiguchi, T. Naito, Alkaloids 50 (1998) 317–342, doi:10.1016/S1099-4831(08)60046-2.
[7] Z.S. Saify, F.I.M. Vaid, Pak. J. Pharm. Sci. 11 (1998) 15–21 http://www.pjps.pk/wp-content/uploads/pdfs/CD-PJPS-11-1-98/Paper-3.pdf.
[8] P.A. Reddy, K.E. Woodward, S.M. McIlheran, B.C. Hsiang, T.N. Latifi, M.W. Hill, S.M. Rothman, J.A. Ferrendelli, D.F. Covey, J. Med. Chem. 40 (1997) 44–49, doi:10.1021/jm960561u.
[9] J.P. Jasinski, R.J. Butcher, H.S. Yathirajan, L. Mallesha, K.N. Mohana, Acta Crystallogr. Section E: Struct. Rep. Online 65 (10) (2009) o2365–o2366, doi:10.1107/S1600536811017855.
[10] S. Grant, A. Fittton, Drugs 48 (1994) 253–273, doi:10.2165/00003495-199448020-00009.
[11] A. Szarfman, J.M. Tonning, J.G. Levine, P.M. Doraiswamy, Pharmacotherapy 26 (2006) 748–758, doi:10.1592/phco.26.6.748.
[12] O. Ostroverkhova, Chem. Rev. 116 (22) (2016) 13279–13412, doi:10.1021/acs.chemrev.6b00127.
[13] P. Yu, Y. Zhen, H. Dong, W. Hu, Chem. 5 (11) (2019) 2814–2853, doi:10.1016/j.chempr.2019.08.019.
[14] S.K. Park, J.H. Kim, S.Y. Park, Adv. Mater. 30 (2018) 1704759, doi:10.1002/adma.201704759.
[15] R. Li, W. Hu, Y. Liu, D. Zhu, Acc. chem. Res. 43 (4) (2010) 529–540, doi:10.1021/ar900228v.
[16] X. Zhang, H.L. Dong, W.P. Hu, Adv. Mater. 30 (2018) 1801048, doi:10.1002/adma.201801048.
[17] C. Wang, H. Dong, L. Jiang, W. Hu, Chem. Soc. Rev. 47 (2) (2018) 422–500, doi:10.1039/C7CS00490G.
[18] L. Mallesha, K.N. Mohana, Can. Chem. Trans. 2 (2014) 343–352, doi:10.13179/canchemtrans.2014.02.03.0121.
[19] Bruker- SAINT PLUS, Bruker AXS Inc., Madison, Wisconsin, (2012) USA.
[20] G.M. Sheldrick, Acta Cryst., C 71 (2015) 3–8, doi:10.1107/S2053229614024218.
[21] G.M. Sheldrick, Acta Cryst., A 46 (6) (1990) 467–473, doi:10.1107/S0108767390000277.
[22] A.L. Spek, Acta. Cryst. A. 46 (1990) 34 https://scripts.iucr.org/cgi-bin/paper?a29681.
[23] C.F. Macrae, I.J. Bruno, J.A. Chisholm, P.R. Edgington, P. McCabe, E. Pidcock, L.M. Rodriguez, R. Taylor, J. van de Streek, P.A. Wood, J. Appl. Cryst. 41 (2008) 466–470, doi:10.1107/S0021889807067908.
[24] M.J. Frisch, G.W. Trucks, H.B. Schlegel, G.E. Scuseria, M.A. Robb, J.R. Cheeseman, G. Scalmani, V. Barone, B. Mennucci, G.A. Petersson, H. Nakatsuji, M. Caricato, X. Li, H.P. Hratchian, A.F. Izmaylov, J. Bloino, G. Zheng, J.L. Sonnenberg, M. Hada, M. Ehara, K. Toyota, R. Fukuda, J. Hasegawa, M. Ishida, T. Nakajima, Y. Honda, O. Kitao, H. Nakai, T. Vreven, J.A. Montgomery Jr., J.E. Peralta, F. Ogliaro, M. Bearpark, J.J. Heyd, E. Brothers, K.N. Kudin, V.N. Staroverov, T. Keith, R. Kobayashi, J. Normand, K. Raghavachari, A. Rendell, J.C. Burant, S.S. Iyengar, J. Tomasi, M. Cossi, N. Rega, J.M. Millam, M. Klene, J.E. Knox, J.B. Cross, V. Bakken, C. Adamo, J. Jaramillo, R. Gomperts, R.E. Stratmann, O. Yazyev, A.J. Austin, R. Cammi, C. Pomelli, J.W. Ochterski, R.L. Martin, K. Morokuma, V.G. Zakrzewski, G.A. Voth, P. Salvador, J.J. Dannenberg, S. Dapprich, A.D. Daniels, O. Farkas, J.B. Foresman, J.V. Ortiz, J. Cioslowski, D.J. Fox, Gaussian 09, Revision B.01, Gaussian, Inc., Wallingford, CT, 2010 https://gaussian.com/g16citation/.
[25] C. Lee, W. Yang, R.G. Parr, Phys. Rev. B. 37 (2) (1988) 785–789, doi:10.1103/PhysRevB.37.785.
[26] A.D. Becke, Phys. ReV. A 1988 (38) (1993) 3098 (b) Becke. J. Chem. Phys., 98(1372), 5648, doi:10.1063/1.464913.
[27] I. Warad, F.F. Awwadi, M. Daqqa, A. Al Ali, T.S. Ababneh, T.M. AlShboul, Y.N. Mabkhot, J. Photochem. Photobio. B: Bio. 171 (2017) 9–19, doi:10.1016/j.jphotobiol.2017.04.01.
[28] T. Koopmans, Physica. 1 (1934) 104–113, doi:10.1016/S0031-8914(34)90011-2.
[29] K. Kumara, F.H. Al-Ostoot, Y.H.E. Mohammed, S.A. Khanum, N.K. Lokanath, Chem. Data Coll. 20 (2019) 100195, doi:10.1016/j.cdc.2019.100195.
[30] A. Frisch, R. Dennington, T. Keith, J. Millam, A. Nielsen, A. Holder, J. Hiscocks, GaussView Version 6 User Manual, Gaussian Inc., Wallingford, CT, USA, 2009.
[31] M.J. Turner, J.J. McKinnon, S.K. Wolff, D.J. Grimwood, P.R. Spackman, D. Jayatilaka, M.A. Spackman, CrystalExplorer (Version 17.5), University of Western Australia, 2018.
[32] R. Seck, A. Gassama, S. Cojean, C. Cavé, Molecules 25 (2) (2020) 299–315, doi:10.3390/molecules25020299.
[33] C.S. Karthik, L. Mallesha, M.V. Santhosh, S. Nagashree, P. Mallu, Indian J. Adv. Chem. Sci. S1 (2016) 206–212 https://www.ijacskros.com/artcles/IJACS-2S-43.pdf.
[34] S.V. Dorozhkin, Scanning 17 (6) (1995) 355–360, doi:10.1002/sca.4950170603.
[35] R. Lakshmi, P. Prabukanthan, G. Harichandran, and C. Sudarsana Kumar, Cryst. Res. Technol., 54(1), 1700146. 10.1002/crat.201700146
[36] D. Cremer, J.A. Pople, J. Amer. Chem. Soc. 97 (1975) 1354–1358, doi:10.1021/ja00839a011.
[37] K. Kumara, K.P. Harish, S. Naveen, H.C. Tandon, K.N. Mohana, N.K. Lokanath, Chem. Data Coll. 11 (2017) 40–58, doi:10.1016/j.cdc.2017.07.007.
[38] A. Bassindale, The Third Dimension In Organic Chemistry, New York, (1984).
[39] G.R. Desiraju, T. Steiner, The Weak Hydrogen Bond: In Structural Chemistry And Biology (Vol. 9), International Union of Crystal, 2009.
[40] A.A. Kala, K. Kumara, N.V. Harohally, N.K. Lokanath, J. Mol. Struct. 1202 (2020) 127238, doi:10.1016/j.molstruc.2019.127238.
[41] S. Naveen, K. Kumara, H.M. Al-Maqtari, M.V.D. Urs, J. Jamalis, K.R. Reddy, N.K. Lokanath, Chem. Data Coll. 24 (2019) 100292, doi:10.1016/j.cdc.2019.100292.
[42] V. Kamat, K. Kumara, K. Naik, A. Kotian, P. Netalkar, S. Naveen, V.K. Revankar, J. Mol. Struct. 1149 (2017) 357–366, doi:10.1016/j.molstruc.2017.07.109.
[43] K. Kumara, S. Naveen, L.D. Mahadevaswamy, A.K. Kariyappa, N.K. Lokanath, Chem. Data Coll. 9 (2017) 251–262, doi:10.1016/j.cdc.2016.11.006.
[44] C.R. Martinez, B.L. Iverson, Chem. Sci. 3 (7) (2012) 2191–2201, doi:10.1039/C2SC20045G.
[45] S.K. Seth, J. Mol. Struct. 1064 (2014) 70–75, doi:10.1016/j.molstruc.2014.01.068.
[46] M.A. Spackman, J.J. McKinnon, Cryst. Eng. Comm. 4 (66) (2002) 378–392, doi:10.1039/B203191B.
[47] J.J. McKinnon, D. Jayatilaka, M.A. Spackman, Chem. Comm. 37 (2007) 3814–3816, doi:10.1039/B704980C.
[48] K. Kumara, M. Jyothi, S. Naveen, S.A. Khanum, N.K. Lokanath, Chem. Data Coll. 9 (2017) 152–163, doi:10.1016/j.cdc.2017.06.
[49] S.K. Seth, Cryst. Eng. Comm. 15 (9) (2013) 1772–1781, doi:10.1039/C2CE26682B.
[50] Y.H. Luo, G.G. Wu, S.L. Mao, B.W. Sun, Inorganica Chim. Acta 397 (2013) 1–9, doi:10.1016/j.ica.2012.11.010.
[51] V. Channabasappa, K. Kumara, N.K. Lokanath, A.K. Kariyappa, Chem. Data Coll. 15 (2018) 134–142, doi:10.1016/j.cdc.2018.05.005.

[52] V. Kamat, K. Kumara, S. Shaikh, S. Naveen, N.K. Lokanath, V. Revankar, Chem. Data Coll. 17 (2018) 251–262, doi:10.1016/j.cdc.2018.09.004.
[53] K.L. Jyothi, K. Kumara, M.K. Hema, Raj Gautam Mahesha, T.N. Guru row, N.K. Lokanath, J. Mol. Struct. 1207 (2020) 127828, doi:10.1016/j.molstruc.2020.127828.
[54] C.F. Mackenzie, P.R. Spackman, D. Jayatilaka, M.A. Spackman, IUCrJ 4 (5) (2017) 575–587, doi:10.1107/S205225251700848X.
[55] K. Kumara, A.D. Kumar, S. Naveen, K.A. Kumar, N.K. Lokanath, J. Mol. Struct. 1161 (2018) 285–298, doi:10.1016/j.molstruc.2018.02.068.
[56] K. Kumara, A. Dileep Kumar, K. Ajay Kumar, N.K. Lokanath, Chem. Data Coll. 13-14 (2018) 40–59, doi:10.1016/j.cdc.2018.01.001.
[57] S. Xavier, S. Periandy, S. Ramalingam, Spectrochim. Acta A 137 (2015) 306–320, doi:10.1016/j.saa.2014.08.039.